



A hole-conductor-free, fully printable mesoscopic perovskite solar cell with high stability

Anyi Mei *et al.*

Science **345**, 295 (2014);

DOI: 10.1126/science.1254763

This copy is for your personal, non-commercial use only.

If you wish to distribute this article to others, you can order high-quality copies for your colleagues, clients, or customers by [clicking here](#).

Permission to republish or repurpose articles or portions of articles can be obtained by following the guidelines [here](#).

The following resources related to this article are available online at www.sciencemag.org (this information is current as of July 18, 2014):

Updated information and services, including high-resolution figures, can be found in the online version of this article at:

<http://www.sciencemag.org/content/345/6194/295.full.html>

Supporting Online Material can be found at:

<http://www.sciencemag.org/content/suppl/2014/07/16/345.6194.295.DC1.html>

This article **cites 22 articles**, 4 of which can be accessed free:

<http://www.sciencemag.org/content/345/6194/295.full.html#ref-list-1>

This article appears in the following **subject collections**:

Physics, Applied

http://www.sciencemag.org/cgi/collection/app_physics

PHOTOVOLTAICS

A hole-conductor-free, fully printable mesoscopic perovskite solar cell with high stability

Anyi Mei,^{1*} Xiong Li,^{1*} Linfeng Liu,¹ Zhiliang Ku,¹ Tongfa Liu,¹ Yaoguang Rong,¹ Mi Xu,¹ Min Hu,¹ Jiangzhao Chen,¹ Ying Yang,¹ Michael Grätzel,² Hongwei Han^{1†}

We fabricated a perovskite solar cell that uses a double layer of mesoporous TiO₂ and ZrO₂ as a scaffold infiltrated with perovskite and does not require a hole-conducting layer. The perovskite was produced by drop-casting a solution of PbI₂, methylammonium (MA) iodide, and 5-ammoniumvaleric acid (5-AVA) iodide through a porous carbon film. The 5-AVA templating created mixed-cation perovskite (5-AVA)_x(MA)_{1-x}PbI₃ crystals with lower defect concentration and better pore filling as well as more complete contact with the TiO₂ scaffold, resulting in a longer exciton lifetime and a higher quantum yield for photoinduced charge separation as compared to MAPbI₃. The cell achieved a certified power conversion efficiency of 12.8% and was stable for >1000 hours in ambient air under full sunlight.

Organic-inorganic metal halide perovskite mesoscopic solar cells (1–3) have rapidly reached conversion efficiencies over 15% (4, 5), and most use a methylammonium lead halide (MAPbX₃, X = halogen) and its mixed-halide crystal analog (6–14). These perovskites have a large absorption coefficient, high carrier mobility, direct band gap, and high stability. They are composed of Earth-abundant materials and can be deposited by low-temperature solution methods. However, perovskite crystallization from solution produces large morphological variations (14) and incomplete filling of the mesoporous oxide scaffold, which results in an unwanted spread of the photovoltaic performance of the resulting devices. Most devices use gold as a back contact, in conjunction with organic hole conductors acting as electron-blocking layers. Hole conductors such as the widely used arylamine *spiro*-OMeTAD are not only expensive but can limit the long-term stability of the device. Hole-conductor-free perovskite photovoltaics were initially reported by Etgar *et al.* (15), and to date power conversion efficiencies (PCEs) of 10.85% (16–18) have been achieved, with gold as a counter-electrode.

We fabricated a solar cell using a double layer of mesoporous TiO₂ and ZrO₂ covered by a porous carbon film. The metal halide perovskite was infiltrated into the porous TiO₂/ZrO₂ scaffold by drop-casting a solution through the printed carbon layer that contained PbI₂ in γ -butyrolactone, together with methylammonium (MA) and 5-aminovaleric acid (5-AVA) cations. 5-AVA replaced

part of the MA cations in the cuboctahedral site of MAPbI₃, forming the new mixed-cation perovskite (5-AVA)_x(MA)_{1-x}PbI₃. The orthorhombic perovskite phase formed in the presence of 5-AVA showed greatly increased PCE compared with the neat analog in a hole-conductor-free cell that used a simple mesoscopic TiO₂/ZrO₂/C triple layer as a scaffold to host the perovskite absorber. The role of 5-AVA cations was to template the formation of perovskite crystals in the mesoporous oxide host and induce preferential growth in the normal direction. The resulting mixed-cation perovskite (5-AVA)_x(MA)_{1-x}PbI₃ has better surface contact with the TiO₂ surface and lower defect concentration than the single-cation form MAPbI₃, resulting in improved conversion efficiency. The

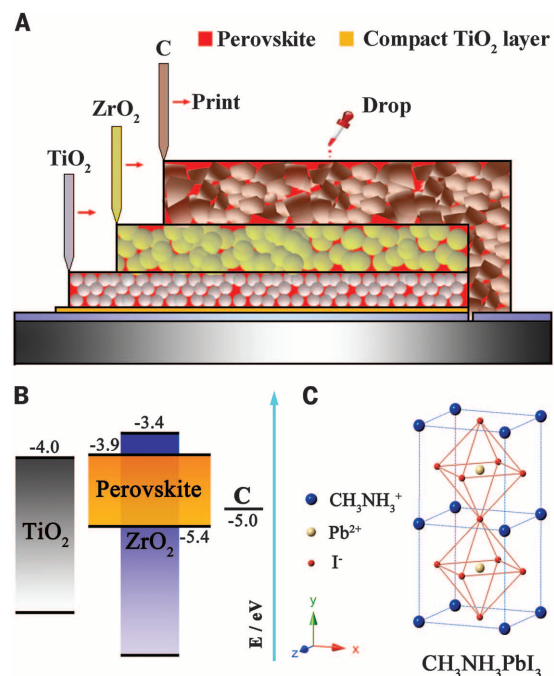
triple-layer device also exhibits excellent long-term stability.

A schematic cross section of the triple-layer, perovskite-based, fully printable mesoscopic solar cell (Fig. 1A) shows that the mesoporous layers of TiO₂ and ZrO₂ have thicknesses of ~1 and 2 μ m, respectively, that were deposited on a F-doped SnO₂ (FTO)-covered glass sheet. The mesoporous layers were infiltrated with perovskite by drop-casting from solution through a 10- μ m-thick carbon layer printed on top of the ZrO₂. The energy band alignment of the device (Fig. 1B) prevents electrons, injected from the photoexcited perovskite into the TiO₂ scaffold, from reaching the back contact because of the 0.6-eV offset between its conduction band and that of ZrO₂. The compact TiO₂ layer deposited on the FTO conducting glass prevents the valence band holes from reaching the FTO-covered front electrode. The CH₃NH₃PbI₃ perovskite unit cell (Fig. 1C) contains one Pb²⁺, one organic ammonium cation, and three I⁻ anions (19).

We introduced the 5-AVA cation into the perovskite lattice with a mixture of MA and 5-AVA in the precursor solution that maintained a 1:1 molar ratio of organic ammonium cations and PbI₂. The optimal molar ratio of ammonium cations (5-AVA)_x(MA)_{1-x}PbI₃ was determined to be between 1:20 and 1:30. The x-ray diffraction (XRD) patterns of neat MAPbI₃ and (5-AVA)_x(MA)_{1-x}PbI₃ infiltrated into the mesoporous ZrO₂/TiO₂ film are compared in Fig. 2. The newly emerging diffraction peaks arising from the (001) and (111) lattice planes for (5-AVA)_x(MA)_{1-x}PbI₃ are much stronger than the corresponding ones for MAPbI₃. And even at low 5-AVA/MA molar ratios, 5-AVA substantially increases the *b* and *c* lattice parameters. The large expansion of the *c* axis induced by 5-AVA indicates its preferential alignment along this axis through contact with lead and

Fig. 1. The triple-layer perovskite junction.

(A) Schematic drawing showing the cross section of the triple-layer perovskite-based fully printable mesoscopic solar cell. The mesoporous layers of TiO₂ and ZrO₂ have a thickness of ~1 and 2 μ m, respectively, and are deposited on a FTO-covered glass sheet shown in blue and gray. They are infiltrated with perovskite by drop-casting from solution. (B) Energy band diagram of the triple-layer device. Energies are expressed in electron volts, using the electron energy in vacuum as a reference. The energy levels of the conduction band edges of TiO₂, ZrO₂, and MAPbI₃ are at -4.0, -3.4, and -3.9 eV, respectively, whereas the valence band edge of the perovskite is at -5.4 eV and that of the Fermi level of carbon is at -5.0 eV. (C) The crystal structure of MAPbI₃ perovskite.



¹Michael Grätzel Center for Mesoscopic Solar Cells, Wuhan National Laboratory for Optoelectronics, School of Optical and Electronic Information, Huazhong University of Science and Technology, Wuhan 430074, Hubei, People's Republic of China. ²Laboratory for Photonics and Interfaces, Institute of Chemical Sciences and Engineering, School of Basic Sciences, Ecole Polytechnique Federale de Lausanne, CH-1015 Lausanne, Switzerland.

*These authors contributed equally to this work. †Corresponding author. E-mail: hongwei.han@mail.hust.edu.cn

iodide ions, and the *c* axis becomes the dominant orientation during crystal growth. Mercier (20) used 4-ammonium-butyric acid (4-ABA) as a template for the engineering of (4-ABA)₂PbI₄ and mixed-cation (4-ABA)₂MAPb₂I₇ perovskite crystals. The ABA molecules formed linear hydrogen-bonded chains that act as supramolecular synthons for layered plumbiodide perovskite structures. We propose that the 5-AVA affects the crystal growth of (5-AVA)_x(MA)_{1-x}PbI₃ in a similar fashion through the formation of hydrogen bonds between its COOH and NH₃⁺ groups and I⁻ ions from the PbI₆ octahedra.

We applied transmission electron microscopy (TEM) and scanning electron microscopy (SEM) to unravel differences in the morphology of the two perovskites. High-resolution TEM images (Fig. 3, A to C) reflecting the morphology of neat TiO₂ particles, as well as MAPbI₃ or (5-AVA)_x(MA)_{1-x}PbI₃-covered TiO₂ particles that were scraped off of mesoporous TiO₂ films infiltrated with MAPbI₃ or (5-AVA)_x(MA)_{1-x}PbI₃, respectively. Substantial differences appeared between the morphologies of the samples produced from the two different perovskite precursor solutions. The observed pattern indicates that there is a much denser coverage of the TiO₂ particles with (5-AVA)_x(MA)_{1-x}PbI₃ as compared to MAPbI₃. The (5-AVA)_x(MA)_{1-x}PbI₃ appears to exhibit crystalline features on a much longer length scale than MAPbI₃, covering most of the TiO₂ surface in a uniform fashion. In contrast, the single-step solution precipitation of MAPbI₃ only partially coated the substrate and left large areas where the perovskite absorber was completely absent. The improvement of the perovskite crystal quality and the higher loading of the mesopores of the oxide scaffold in the presence of 5-AVA cations probably resulted from the templating action of the AVA affecting the perovskite crystal nucleation and growth within the mesoscopic oxide scaffold. The COOH groups of 5-AVA anchor a monolayer of the amino acid to the surface of the mesoporous TiO₂ and ZrO₂ film by coordinative binding to the exposed Ti(IV) or Zr(IV) ions. In the adsorbed state, the terminal -NH₃⁺ groups of 5-AVA face the perovskite solution and hence serve as nucleation sites. This role we attribute to AVA is confirmed by recent work (21) showing that protonated amino acids of the AVA type indeed template the crystal growth of plumbihalide perovskites in mesoscopic TiO₂ films, improving the crystalline network and charge-carrier lifetime of the CH₃NH₃PbI₃ inserted into the porous metal oxides.

We performed photoluminescence (PL) decay measurements in order to extract quantitative information on the yield of light-induced charge separation. Excitons generated by light excitation of MAPbI₃ dissociate into free charge carriers within 1 ps (22). We infiltrated mesoporous TiO₂ and ZrO₂ films with MAPbI₃ or (5-AVA)_x(MA)_{1-x}PbI₃ and measured the PL decay; ZrO₂ serves as a reference because its conduction band is not accessible for electron injection. The PL decay of the MAPbI₃ perovskite contained in ZrO₂ films exhibits a time constant of $\tau_c = 8.14$ ns,

Fig. 2. Diffraction data. XRD patterns of mesoscopic ZrO₂/TiO₂ film on FTO glass infiltrated with the perovskites (5-AVA)_x(MA)_{1-x}PbI₃ (red trace) and MAPbI₃ (blue trace), as well as a blank ZrO₂/TiO₂ film (black trace).

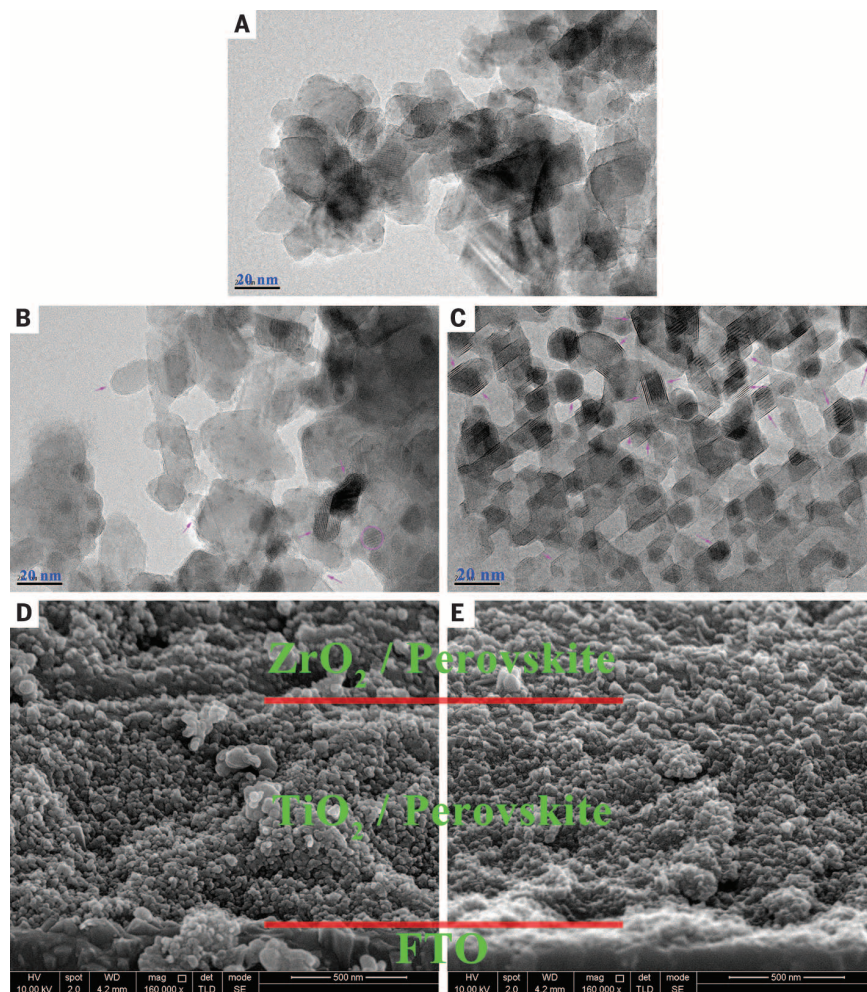
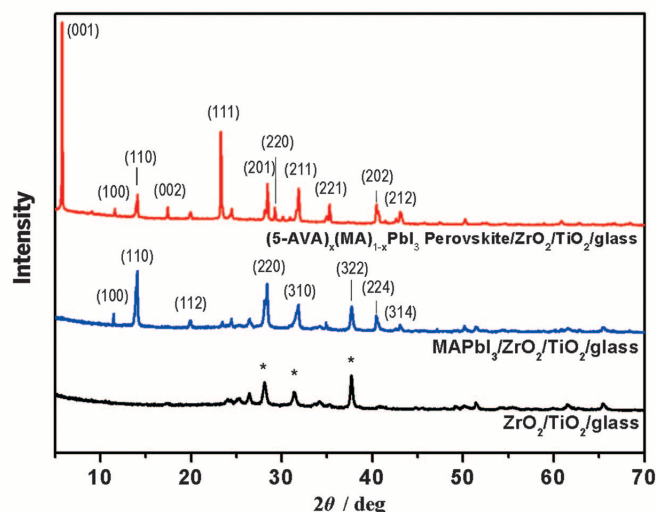
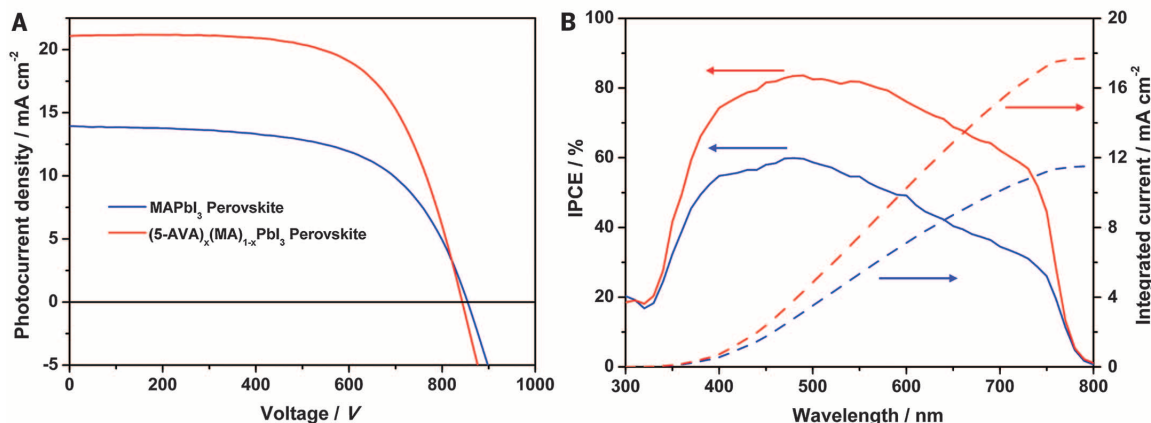


Fig. 3. Microscopy images. (A to C) TEM images of (A) TiO₂ and mixtures of (B) MAPbI₃ and (C) (5-AVA)_x(MA)_{1-x}PbI₃, with TiO₂ particles scraped off of a mesoporous film infiltrated with perovskites. (D and E) SEM images of the cross section of (D) MAPbI₃- and (E) (5-AVA)_x(MA)_{1-x}PbI₃-based perovskite mesoscopic solar cells.

Fig. 4. Device performance. (A)

J - V curves under simulated AM 1.5 solar irradiation at an intensity of 100 mW cm^{-2} measured at room temperature. (B) IPCE curves taken with monochromatic light without applied white-light bias for $(5\text{-AVA})_x(\text{MA})_{1-x}\text{PbI}_3$ (red curve) or MAPbI_3 (blue curve). The integrated photocurrents calculated from the

overlap integral of the IPCE spectra with the AM 1.5 solar emission are also shown. The integrated photocurrent of the $(5\text{-AVA})_x(\text{MA})_{1-x}\text{PbI}_3$ -based photovoltaic is 17.8 mA cm^{-2} , which agrees closely with the photocurrent density of 18.4 mA cm^{-2} measured at the beginning of testing, which rose to 21.1 mA cm^{-2} after 3 min of light soaking.



whereas for the $(5\text{-AVA})_x(\text{MA})_{1-x}\text{PbI}_3$, τ_e is **23.7 ns** [fig. S1 (23)]. The longer charge-carrier lifetime observed with $(5\text{-AVA})_x(\text{MA})_{1-x}\text{PbI}_3$ indicates a much lower defect concentration. With the TiO_2 scaffold, τ_e for MAPbI_3 and $(5\text{-AVA})_x(\text{MA})_{1-x}\text{PbI}_3$ were similar, 1.71 and 1.36 ns, respectively; and from the branching ratios, led to calculated quantum efficiencies of 94 and 80%, respectively.

Cross-sectional SEM views of the $(5\text{-AVA})_x(\text{MA})_{1-x}\text{PbI}_3$ - and MAPbI_3 -based mesoscopic solar cells, which confirm the different extent of pore filling by the two perovskites are shown in Fig. 3, D and E. Thus, for $(5\text{-AVA})_x(\text{MA})_{1-x}\text{PbI}_3$, most of the mesopores of the $\text{ZrO}_2/\text{TiO}_2$ double layer are fully loaded with the perovskite, whereas for the device with MAPbI_3 , the pore filling is less complete, with a substantial amount of voids remaining within the mesoporous $\text{ZrO}_2/\text{TiO}_2$ double-layer film. Optical studies also confirmed the higher perovskite loading in the presence of 5-AVA [figs. S2 and S3 (23)].

We measured the photocurrent density as a function of forward bias voltage (J - V curves) of the $(5\text{-AVA})_x(\text{MA})_{1-x}\text{PbI}_3$ - and the MAPbI_3 -based mesoscopic solar cells under standard reporting conditions [air mass 1.5 (AM1.5) global solar light at 100 mW cm^{-2} and room temperature]. Figure S4 (23) presents the temporal evolution of the device performance for $(5\text{-AVA})_x(\text{MA})_{1-x}\text{PbI}_3$ -based mesoscopic solar cells during the initial phase of illumination. The four key photovoltaic parameters; i.e., the open-circuit voltage (V_{oc}), short-circuit photocurrent (J_{sc}), fill factor (FF), and PCE, increased to a stable value within the first 3 min and then exhibited excellent stability during exposure to full AM 1.5 simulated sunlight over 1008 hours. The final PCE increased slightly during this period, which is more remarkable given that the test was performed with an unsealed device, the perovskite being protected by the $10\text{-}\mu\text{m}$ -thick carbon layer back contact acting as a water-retaining layer.

A hysteresis effect often appears during measurement of the J - V curves of perovskite solar cells. For a mesoscopic triple-layer solar cell with perovskite $(5\text{-AVA})_x(\text{MA})_{1-x}\text{PbI}_3$ under standard

1 sun irradiation with the scanning rate of 3 mV s^{-1} , there was no substantial effect [fig. S5 (23)]. However, a hysteresis effect appeared at higher scan rates unless the cell was subjected to light soaking for a few minutes, which eliminated the hysteresis effects even at scan rates as high as 250 mV s^{-1} . The perovskite systems show mixed **ionic and electronic conduction** (24), and under illumination an electric field is set up, which causes a slow drift of ions through the perovskite device to screen the space charge that is generated by light. Figure 4A presents J - V curves collected after 3 min of light soaking with simulated sunlight. In keeping with our previous work (19), the optimized MAPbI_3 -based heterojunction perovskite solar cell produced a J_{sc} of 13.9 mA cm^{-2} , a V_{oc} of 855 mV, and a FF of 0.61, yielding a PCE of 7.2%. The $(5\text{-AVA})_x(\text{MA})_{1-x}\text{PbI}_3$ -based cells showed greatly improved performance, with J_{sc} , V_{oc} , and FF reaching values of 21.1 mA cm^{-2} , 843 mV, and 0.65, respectively, corresponding to a PCE of 11.6%. We sent one of our cells to an accredited photovoltaic calibration laboratory for certification, which measured a J_{sc} value of 22.8 mA cm^{-2} [fig. S6 (23)]. The V_{oc} of the device was 858 mV and the FF was 0.66, corresponding to a PCE of 12.84%. Our certified photocurrent density is superior to values reported so far for any perovskite-based photovoltaic, for which the highest certified J_{sc} is 21.3 mA cm^{-2} (4). Also in Fig. 4A, the slope of the J - V curve at open circuit voltage is steeper for $(5\text{-AVA})_x(\text{MA})_{1-x}\text{PbI}_3$ perovskite than for MAPbI_3 , suggesting a lower series resistance and higher electric conductivity for the former than for the latter perovskite. This shows the better connectivity of the AVA template perovskite crystals formed in the porous oxide network.

In the absence of ZrO_2 , the performance of the perovskite photovoltaic is poor, with $J_{sc} = 12.51 \text{ mA cm}^{-2}$, $V_{oc} = 592 \text{ mV}$, FF = 0.56, and PCE = 4.18% [fig. S7 (23)]. **This confirms that ZrO_2 is blocking the flow of photogenerated electrons to the back contact, preventing recombination with the holes from the perovskite at the back contact.**

Figure S8 (23) reports statistical data concerning the numerical distribution of the key photovoltaic parameters; i.e., V_{oc} , J_{sc} , FF, and PCE for a random selection of 20 photovoltaic devices, which were fully printed on a $10 \text{ cm} \times 10 \text{ cm}$ FTO glass as shown by the photograph in fig. S9 (23). $(5\text{-AVA})_x(\text{MA})_{1-x}\text{PbI}_3$ -based mesoscopic solar cells exhibited an average PCE value of 10.3%, J_{sc} of 21.68 mA cm^{-2} , V_{oc} of 740 mV, and FF of 0.64 together with a small standard deviation, indicating that the $(5\text{-AVA})_x(\text{MA})_{1-x}\text{PbI}_3$ strongly augments the reproducibility of the perovskite-based cells. Figure 4B shows the incident photon-to-electric current conversion efficiency (IPCE), defined as the number of photogenerated charge carriers contributing to the photocurrent per incident photon. These experiments used monochromatic light without applying a white-light bias. $(5\text{-AVA})_x(\text{MA})_{1-x}\text{PbI}_3$ achieved much higher IPCEs than MAPbI_3 over the whole spectral range between 300 and 800 nm, matching the difference in photocurrents obtained for the two devices.

REFERENCES AND NOTES

- G. Hodes, *Science* **342**, 317–318 (2013).
- G. Xing et al., *Science* **342**, 344–347 (2013).
- S. D. Stranks et al., *Science* **342**, 341–344 (2013).
- J. Burschka et al., *Nature* **499**, 316–319 (2013).
- M. Liu, M. B. Johnston, H. J. Snaith, *Nature* **501**, 395–398 (2013).
- J. H. Noh, S. H. Im, J. H. Heo, T. N. Mandal, S. I. Seok, *Nano Lett.* **13**, 1764–1769 (2013).
- H. S. Kim et al., *Nano Lett.* **13**, 2412–2417 (2013).
- H. S. Kim et al., *Nat. Commun.* **4**, 2242 (2013).
- H. Cai, J. B. Dunn, Z. Wang, J. Han, M. Q. Wang, *Biotechnol. Biofuels* **6**, 141 (2013).
- J. H. Heo et al., *Nat. Photonics* **7**, 486–491 (2013).
- A. Abrusci et al., *Adv. Funct. Mater.* **21**, 2571–2579 (2011).
- M. M. Lee, J. Teuscher, T. Miyasaka, T. N. Murakami, H. J. Snaith, *Science* **338**, 643–647 (2012).
- H. S. Kim et al., *Sci. Rep.* **2**, 591 (2012).
- G. E. Eperon, V. M. Burlakov, P. Docampo, A. Goriely, H. J. Snaith, *Adv. Funct. Mater.* **24**, 151–157 (2014).
- L. Etgar et al., *J. Am. Chem. Soc.* **134**, 17396–17399 (2012).
- W. A. Laban, L. Etgar, *Energy Environ. Sci.* **6**, 3249–3253 (2013).
- S. Aharon, S. Gamliel, B. El Cohen, L. Etgar, *Phys. Chem. Chem. Phys.* **16**, 10512–10518 (2014).
- J. Shi et al., *Appl. Phys. Lett.* **104**, 063901 (2014).
- Z. Ku, Y. Rong, M. Xu, T. Liu, H. Han, *Sci. Rep.* **3**, 3132 (2013).
- N. Mercier, *CrystEngComm* **7**, 429 (2005).
- Y. Ogomi et al., *J. Phys. Chem. C* **10.1021/jp412627n** (2014).

22. C. S. Ponceca Jr. et al., *J. Am. Chem. Soc.* **136**, 5189–5192 (2014).
 23. See the supplementary materials on Science Online.
 24. C. C. Stoumpos, C. D. Malliakas, M. G. Kanatzidis, *Inorg. Chem.* **52**, 9019–9038 (2013).

ACKNOWLEDGMENTS

The authors acknowledge financial support from the Ministry of Science and Technology of China (863 project, grant no.

SS2013AA50303), the National Natural Science Foundation of China (grant no. 61106056), the Science and Technology Department of Hubei Province (grant no. 2013BAA090), and the Fundamental Research Funds for the Central Universities (grant no. HUSTNY022). We thank the Analytical and Testing Center of Huazhong University of Science and Technology for field emission SEM, TEM, and XRD testing. M.G. thanks the European Research Council for financial support under advanced research grant ARG 247404, “Mesolight.”

SUPPLEMENTARY MATERIALS

www.sciencemag.org/content/345/6194/295/suppl/DC1
 Materials and Methods
 Supplementary Text
 Figs. S1 to S9
 References

14 April 2014; accepted 3 June 2014
 10.1126/science.1254763

APPLIED OPTICS

Dielectric gradient metasurface optical elements

Dianmin Lin,^{1*} Pengyu Fan,^{1*} Erez Hasman,² Mark L. Brongersma^{1†}

Gradient metasurfaces are two-dimensional optical elements capable of manipulating light by imparting local, space-variant phase changes on an incident electromagnetic wave. These surfaces have thus far been constructed from nanometallic optical antennas, and high diffraction efficiencies have been limited to operation in reflection mode. We describe the experimental realization and operation of dielectric gradient metasurface optical elements capable of also achieving high efficiencies in transmission mode in the visible spectrum. Ultrathin gratings, lenses, and axicons have been realized by patterning a 100-nanometer-thick Si layer into a dense arrangement of Si nanobeam antennas. The use of semiconductors can broaden the general applicability of gradient metasurfaces, as they offer facile integration with electronics and can be realized by mature semiconductor fabrication technologies.

The field of nanophotonics has started to facilitate the replacement of bulky optical components by ultrathin, planar elements (1–5). Such elements can be realized by nanopatterning thin films and can benefit from a more natural integration into electronic and mechanical systems. They can also provide entirely new functions that capitalize on the rapid developments in the field of metamaterials (6). The recent realization of metasurfaces, or metamaterials of reduced dimensionality (7), is of particular relevance as it is opening up new opportunities to realize virtually flat optics (8, 9). Metasurfaces consist of dense arrangements of resonant optical antennas. The resonant nature of the light-matter interaction with such structures affords substantial control over the local light scattering amplitude and phase. These scattering properties can be manipulated through choices of the antenna material, size, geometry, orientation, and environment. By arranging antennas with distinct scattering properties on a surface, space-variant metasurfaces are created that offer tremendous freedom in manipulating optical wave-fronts. Metasurfaces constructed from high-index antenna arrays are used as anti-reflection coatings (10), as well as to enhance absorption (11), create structural color (12), and

manipulate the state of polarization (13, 14). However, space-variant metasurfaces for beam steering and focusing have thus far been constructed from nanoscale metallic antennas only (7). Ohmic losses in the metal and the limited scattering cross sections of the antennas have limited high device efficiencies to reflection mode (15, 16). We leverage recent advances in the realization of high-index dielectric antennas (12, 17, 18) and Pancharatnam-Berry phase optical elements (PBOEs) (19, 20) to realize easy-to-fabricate and highly efficient transmissive devices. Si-based gradient metasurfaces capable of serving as optical gratings, lenses, and axicons are demonstrated.

Figure 1 shows a dielectric gradient metasurface optical element (DGMOE) serving as an axicon. Whereas conventional glass axicons are a few millimeters in size (Fig. 1A), the DGMOE features a 100-nm-thick layer of poly-silicon deposited on a quartz substrate (Fig. 1B) generated in a single patterning step (21). Figure 1D shows a scanning electron microscopy (SEM) image of the fabricated DGMOE composed of thousands of Si nanobeam antennas.

When illuminated with a collimated Gaussian left circularly polarized (LCP) light beam at a 550-nm wavelength, the DGMOE creates a non-diffracting Bessel beam on the transmission (Fig. 1, C and E, and section S2 of the supplementary materials). The intensity distributions along and across the center of Bessel beam are shown as insets to Fig. 1E. The ratio between the high-intensity central beam spot and the first ring is 6:1, a signature of a Bessel beam. The operation of the lens could be analyzed by understanding

all of the coherent far-field and near-field interactions between the Si nanobeam antennas. Here, we describe the behavior of the optical element based on an understanding of the Pancharatnam-Berry (PB) phase.

The PB phase is a geometric phase achieved by space-variant polarization manipulations (22, 23), as opposed to a propagation phase. PBOEs are constructed from wave plate elements for which the orientation of the fast axes depends on the spatial position. Well-defined algorithms exist for realizing specific optical functions. By tiling a surface with half-wave plates with their fast-axes orientations according to a function $\theta(x, y)$, an incident circularly polarized light beam will be fully transformed to a beam of opposite helicity and imprinted with a geometric phase equal to $\varphi_g(x, y) = \pm 2\theta(x, y)$ (21, 24). By controlling the local orientation of the fast axes of the wave plate elements between 0 and π , phase pickups can be achieved that cover the full 0-to- 2π range while maintaining equal transmission amplitude for the entire optical component. This provides full control over the wavefront. A continuous desired phase function can be approximated using discrete wave plate orientations. We use eight orientations with which a high theoretical diffraction efficiency of 95% can be achieved (25). The realization of wave plate elements represents a crucial step in crafting PBOEs.

In designing ultrathin nanobeam-based wave plates, it is important to first understand the optical resonances of individual semiconductor nanobeams. Top-illuminated single beams support resonances under transverse electric (TE) illumination (with the electric field polarized normal to the length of the structure) and the orthogonal transverse magnetic (TM) polarization (12, 18). The thickness of the resonant structures can be small compared with the free-space wavelength due to the high refractive index of semiconductors. A 120-nm-wide and 100-nm-high Si nanobeam supports a strong resonance and a substantial phase retardation in our target wavelength range of interest. We chose this beam as the basic building block for our wave plate (Fig. 2A) in anticipation that its resonant behavior and the accompanied phase retardation between the orthogonal polarizations would persist in the beam array. Finite element simulations indicate that the wavefront for a TE-polarized light beam at 550 nm is delayed by 0.14π as compared with the wavefront in the absence of the nanobeams. The wavefront for TM-polarized light is delayed even further to 1.15π (Fig. 2B). As a result, the phase retardation between the two orthogonal polarizations

¹Geballe Laboratory for Advanced Materials, Stanford University, 476 Lomita Mall, Stanford, CA 94305, USA.

²Micro and Nanooptics Laboratory, Faculty of Mechanical Engineering and Russell Berrie Nanotechnology Institute, Technion-Israel Institute of Technology, Haifa 32000, Israel.

*These authors contributed equally to this work. †Corresponding author. E-mail: brongersma@stanford.edu